Improved Target Stability Using Picket Pulses to Increase and Shape the Ablator Adiabat

Introduction

The minimum energy required for ignition of the imploding capsule in inertial confinement fusion[1] is a strong function of the fuel adiabat α_{stag} (the ratio of the shell pressure to the Fermi-degenerate pressure) at the time of maximum compression: $E_{\min} \sim a_{\text{stag}}^{1.9}$ (Refs. 2 and 3). The shell must be driven on the lowest-possible adiabat to minimize this energy. The performance of low-adiabat implosions is limited by hydrodynamic instabilities that tend to disrupt the shell during the acceleration phase. The most important instability is the Rayleigh–Taylor[4,5] (RT) instability that is seeded by single-beam nonuniformities and surface roughness. The RT growth is reduced by mass ablation from the target surface[6–9] characterized by the ablation velocity V_a.

Interface perturbations grow exponentially ($a = a_0 e^{\gamma t}$) during the "linear" phase of the RT instability and reach a saturation phase (when $a \sim \lambda/10$) where the growth continues at a reduced rate.[10] Here, a is the amplitude of the perturbation, a_0 is the initial perturbation amplitude (the seed), γ is the growth rate, and λ is the wavelength of the perturbation.

A great deal of effort has gone into reducing the seeds (a_0) caused by illumination nonuniformities (imprinting) and target imperfections. The effect of imprinting has been reduced by a number of beam-smoothing techniques, including distributed phase plates (DPP's),[11] polarization smoothing (PS) with birefringent wedges,[12,13] smoothing by spectral dispersion (SSD),[14] and induced spatial incoherence (ISI).[15] The effect of the RT instability can also be reduced by lowering the RT growth rate. It has been shown that the ablation-surface RT growth rate is reduced by the ablation process. Theoretical work that includes the effect of thermal transport[9] shows that the RT-growth-rate dispersion formula for a DT target is given by

$$\gamma_{\text{DT}} = \sqrt{A_T\left(L_0,\nu\right)kg - A_T^2\left(L_0,\nu\right)k^2 V_a V_{bo}}$$

$$-\left[1 + A_T\left(L_0,\nu\right)\right]kV_a,$$

where $A_T(L_0,\nu)$ is the Atwood number, a function of L_0 and ν; k is the perturbation spatial wave number; g is acceleration; L_0 is ablation interface thickness; V_a is ablation velocity; V_{bo} is the "blowoff" velocity; and ν is the thermal transport index. V_{bo} is equal to V_a times the ratio of the blowoff plasma density to the ablation surface density. The ablation velocity, in turn, increases with the adiabat α in the ablation region as $V_a \propto \alpha^{3/5}$ (Ref. 16). This is the compromise that faces target designers—lowering α reduces the minimum energy required for ignition, but increases the effects of the RT instability. This article describes recent results using a shaped adiabat that increases the ablation-surface adiabat while maintaining a low adiabat for the compressed fuel.

This article is divided into five sections: (1) the motivation for adiabat shaping; (2) the results from the planar growth and imprint experiments; (3) data from spherical implosions with the decaying-shock-wave picket and the relaxation picket; (4) simulations showing the extension of the picket pulses to cryogenic implosions; and (5) conclusions.

Adiabat Shaping

The conflicting requirements of the lower-adiabat fuel at the maximum compression and the higher-adiabat ablation region can be achieved by shaping the adiabat inside the shell. A schematic of a shaped shell adiabat is shown in Fig. 101.8, where the shell is represented as a region of constant density and the adiabat varies from 1.5 to 4. The shaded region is the portion of the shell that remains at the end of the acceleration phase of the implosion. The inner fuel region is on a low adiabat while the adiabat in the ablated mass is high. The first published work on adiabat shaping used the absorption of low-energy x rays[17] to increase the adiabat at the ablation surface.

A short, high-intensity picket pulse, as seen in Fig. 101.9(a), can be used to shape the shell adiabat by creating a decaying shock wave.[18,19] This technique modifies the adiabat by modifying the pressure inside the shell. The ablation pressure from the picket pulse creates a shock wave that raises the pressure at the ablation surface and propagates into the shell. A rarefaction wave propagates toward the shock wave at the end of the picket pulse. The shock-wave pressure then decays after the rarefaction wave overtakes it, reducing the pressure and lowering the adiabat for the inner sections of the shell.

The shell adiabat can also be shaped by propagating a strong shock wave in a fluid where the density increases from the ablation surface to the inner shell.[20] This density shape is created by a low-intensity, narrow picket pulse that causes the shell to decompress after it is turned off. This pulse shape is shown in Fig. 101.9(b). Shell decompression creates a density profile that is low at the ablation interface and high in the inner shell. The pulse shape needs to be timed so that the shock wave from the drive pulse reaches the shell–gas interface at the same time as the rarefaction wave from the picket pulse.

Picket-pulse shapes are not new to inertial confinement fusion (ICF); Lindl and Mead mentioned picket pulses in Ref. 21. This work showed that multiple picket pulses used in a simulation showed reduced target distortions during implosion. This was attributed to the impulsive nature of the picket drive with no mention of adiabat shaping. In the 1980s, simulations done at Lawrence Livermore National Laboratory (LLNL) and LLE[22] showed that if a picket pulse is used with a low-adiabat drive, the acceleration RT growth is reduced.

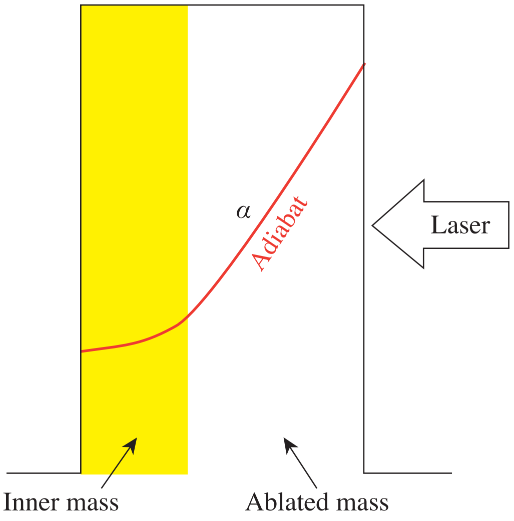

E13530

Figure 101.8
Schematic of a shell showing a shaped adiabat between the ablation surface and the inner surface. The shaded region is the portion of the shell that is not ablated. The adiabat is higher in the ablated material and therefore reduces the RT growth of ablation-interface perturbations.

LLE has done planar RT growth experiments[23] with picket pulses and established an analytical understanding of adiabat shaping with picket pulses.[18–20] Picket pulses are being actively studied to improve direct-drive target performance.

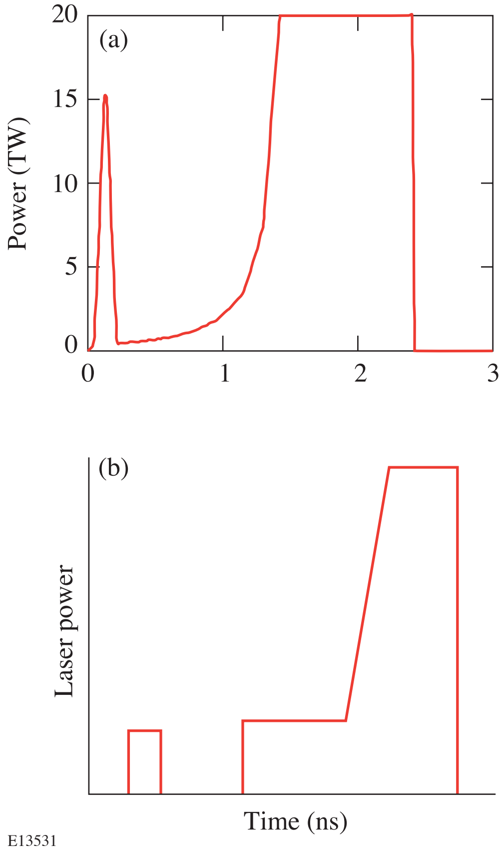

E13531

Figure 101.9
Laser pulse shapes for a decaying-shock-wave picket and a relaxation picket. In (a) the decaying shock wave is created by the short picket at the beginning of the pulse shape. The adiabat is shaped as the shock wave decays. The pulse shape for a relaxation picket drive is shown in (b). The low-intensity, narrow picket in front creates a spatial-density profile that is low at the ablation region and high inside the shell. The strong shock wave resulting from the high foot intensity then propagates through this density profile, shaping the shell's adiabat.

Planar Experiments

Acceleration interface perturbation growth due to the RT instability has been routinely studied in planar targets. A nonconverging planar target allows the whole foil to be placed on a high adiabat to study how the adiabat affects the RT growth. The mass-modulated accelerated foil was composed of a 20-μm-thick CH foil with perturbations imposed on the side irradiated by the laser.[24] This thickness was chosen because it has about two attenuation depths for the 1.0- to 1.5-keV x rays used for radiography. The initial perturbations were (1) a wavelength of $\lambda = 60$ μm and amplitude of $a = 0.25$ μm; (2) $\lambda = 30$ μm and $a = 0.125$ and 0.25 μm; and (3) $\lambda = 20$ μm and $a = 0.05$ and 0.25 μm. The perturbation amplitudes decreased with decreasing wavelength to ensure that the growth was measured in the "linear" ($a < \lambda/10$) phase of the RT instability. The 0.25-μm-amplitude perturbation at wavelengths of 30 μm and 20 μm was used to study the stability of this perturbation for large picket intensities where little or no growth was expected and the smaller amplitude perturbation was below the detection threshold.

Planar targets with imposed mass perturbations were accelerated using ten laser beams overlapped with a total overlapped peak intensity of 1.7×10^{14} W/cm^2. Each of the drive beams was focused to a spot size with a diameter of ~930 μm (at the 5% intensity contour) and used all of the beam smoothing available on OMEGA. The use of distributed phase plates, polarization smoothing, and SSD resulted in a laser-irradiation nonuniformity relative to the intensity envelope of <1% over a 600-μm-diam region defined by the 90% intensity contour. Two pulse shapes were used for the drive beams: first, a pulse with a Gaussian rise to a 2-ns constant intensity (referred to as the drive pulse) and, second, this same pulse with a Gaussian picket placed ~2 ns ahead of the time when the drive pulse reaches constant intensity. The pulse shape is shown in Fig. 101.10(a). The maximum drive intensity was designed to be the same for irradiation with and without a picket.

A comparison of the calculated and measured amplitudes of the fundamental Fourier mode of the optical-depth modulation for a 20-μm-wavelength perturbation is shown in Fig. 101.10(b), for a drive pulse only, a picket 50% of the drive-pulse intensity, and a picket 100% of the drive intensity. The data with and without the picket have been temporally shifted to match the start of the measured drive pulse. Multiple shots were performed at each wavelength, with the x-ray diagnostics using different temporal windows covering the duration of the drive pulse. A clear reduction in the 20-μm-wavelength perturbation growth rate is seen for the 50% I_p/I_d data. Data for a picket with an intensity of 100% of the drive pulse show that the ablation velocity during the drive pulse is large enough to stabilize the RT growth at this wavelength. Two-dimensional (2-D) hydrodynamic simulations of the experiment agree with the experimental data without and with picket pulses with intensities equal to 50% of the drive pulse.

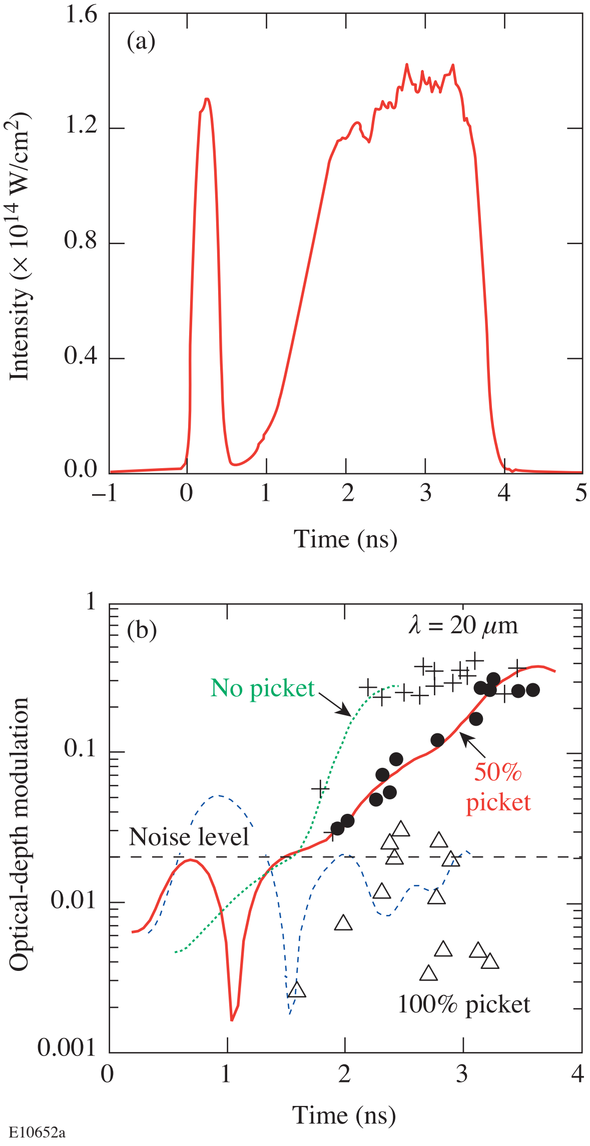

Figure 101.10
Planar RT growth experiments used the pulse shape shown in (a). The 300-ps-wide picket caused the foil to decompress, lowering the ablation-interface density and raising the ablation velocity. The modulation in optical depth is shown in (b) for an imposed 20-μm-wavelength perturbation. Data without a picket are shown as plus (+) symbols, data for a picket with an intensity of 50% of the drive are shown as filled circles, and data for a picket with an intensity of 100% of the drive are shown as triangles. Lines indicate 2-D hydrodynamic simulations of the experiments with the dotted line for no picket, the solid line for a 50% picket, and the dashed line for a 100% picket.

A picket pulse is also effective in reducing the imprint seed for the RT instability in cryogenic implosions.[22] Current cryogenic targets are thin (~3- to 5-μm) CH shells with a 100-μm layer of DT or D_2 ice. The density mismatch between the CH shell and the hydrogenic layer causes a pressure gradient to be established during the constant-intensity foot portion of the laser illumination. The ablation surface is accelerated as a result of the pressure gradient, and the laser imprint is amplified by the RT instability. A picket pulse mitigates the pressure gradient and reduces the RT amplification of the laser nonuniformities and thus reduces the RT seed from imprinting for the target implosion.

Planar experiments were done to study imprint reduction with picket pulses for layered targets. The planar targets were constructed with a 5-μm-thick, solid-density CH layer and a 90-μm-thick CH foam layer with a density of 0.18 g/cm^3. This foil target acts as a surrogate for a section of a cryogenic spherical target. Intensity perturbations with wavelengths of 120, 90, 60, and 30 μm using specifically designed DPP's in a single beam were imposed on these planar foils. Figures 101.11 and 101.12 show the experimental optical-depth-modulation amplitude for these perturbations. Data in Figs. 101.11(a) and 101.11(b) show little reduction in the imprinting for long-

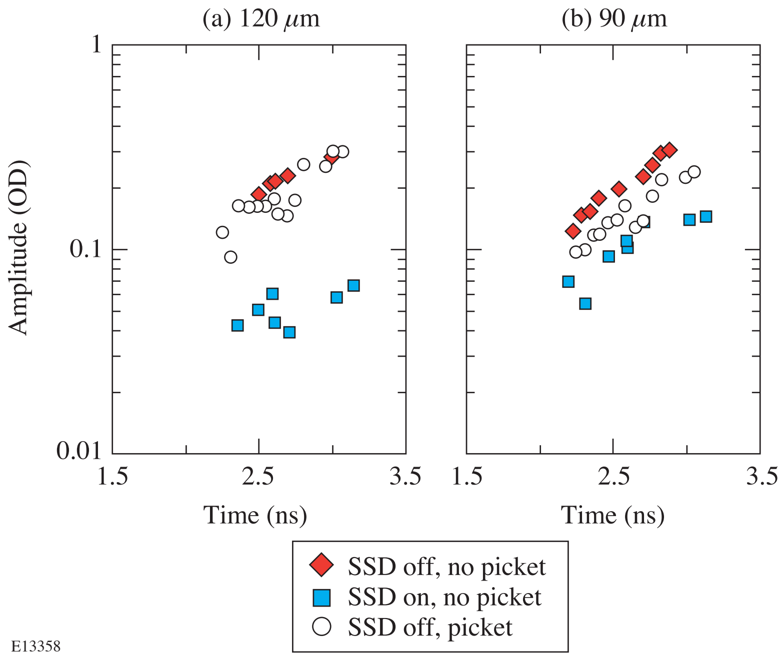

Figure 101.11
Imprinting data for 120-μm and 90-μm intensity perturbations. Data with SSD off and no picket are plotted as diamonds, data with SSD on and no picket as squares, and data with SSD off and with the picket as circles.

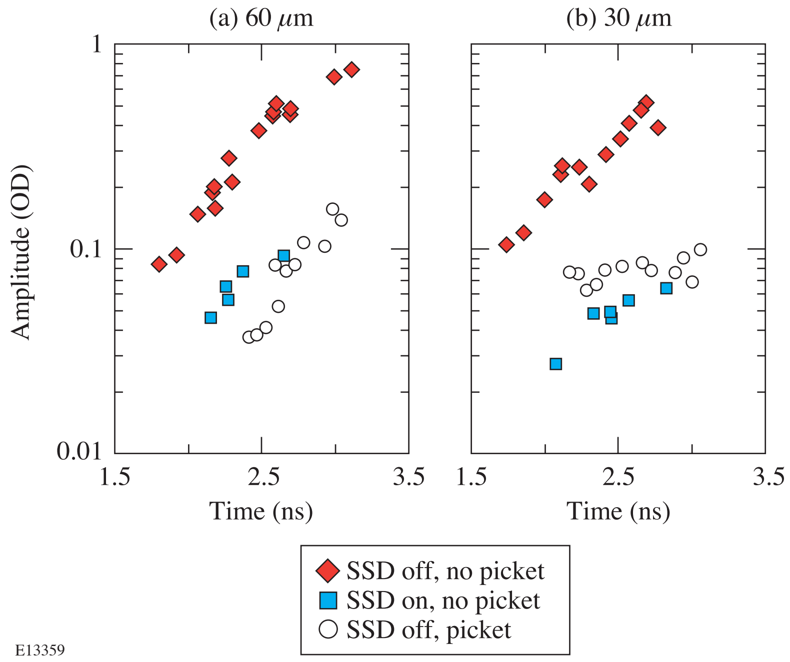

Figure 101.12
Imprinting data for 60-μm and 30-μm intensity perturbations. Data with SSD off and no picket are plotted as diamonds, data with SSD on and no picket as squares, and data with SSD off and with the picket as circles.

wavelength perturbations when the picket pulse was used. There is no difference at 120-μm-wavelength perturbations [Fig. 101.11(a)] with and without the picket. The data for a 90-μm-wavelength perturbation [Fig. 101.11(b)] with the picket pulse lie between the data without the picket and with SSD off and SSD on. The shorter-wavelength perturbations show a greater effect on optical-depth modulation for the picket pulse [Figs. 101.12(a) and 101.12(b)].

Modulation in optical-depth data shows that the amplitude of the imprint with the picket is the same as that when SSD is on and there is no picket pulse. The DPP's used to impose the intensity perturbations are refractive optics, so SSD will not affect the perturbation wavelength but will reduce the contrast and, thus, the perturbation amplitude. The picket is as effective as one-dimentional (1-D), 1.5-Å SSD at reducing the imprint for 60-μm-wavelength [Fig. 101.12(a)] and 30-μm-wavelength [Fig. 101.12(b)] perturbations.

The temporal evolution of the optical-depth data shown in Figs. 101.11 and 101.12 shows that only the 30-μm-wavelength perturbation has its RT growth rate reduced. This is not unexpected. Previous planar growth experiments with picket pulses[20] have shown that the RT growth of long-wavelength perturbations ($\lambda \geq 60$ μm) is less affected by the picket pulse than the short-wavelength perturbations ($\lambda = 30$ and 20 μm). This is a result of the *k*-dependence of the ablation-velocity stabilization term in the dispersion formula for the RT growth rate.

Spherical Experiments

The OMEGA[26] laser system imploded spherical targets with the pulse shapes shown in Fig. 101.13. Sixty beams of 351-nm radiation were incident onto the target. All beams had polarization smoothing, 1-THz bandwidth, 2-D SSD, and DPP's with an intensity envelope given by a third-order super-Gaussian to minimize the illumination nonuniformities imposed by the laser. The targets used for these measurements are shown as the inset in Fig. 101.13. The shells were made of either 33- or 27-μm-thick polystyrene and filled with three gas-fill conditions: 15 atm of D_2; 3 atm of D_2; and a mixture of 12 atm of ^{3}He and 6 atm of D_2. All targets had a 1000-Å layer of aluminum as a gas-retention barrier. The laser pulse shapes were optimized for an outer diameter of 906 μm, and the targets had diameters that ranged from 901 to 923 μm.

Results from the fusion-product-yield measurements for three shots for each target and pulse shape are shown in Figs. 101.14(a) and 101.14(b). For the 15-atm-D_2-filled, 33-μm-thick shell [Fig. 101.14(a)], there is a factor-of-3 increase in the number of D_2 neutrons from the target irradiated with a picket pulse than that from the target without a picket. The experiment was optimized for the 33-μm-thick shells; the improvement for the 27-μm-thick shells is only 50%. Both the 3-atm-D_2-filled and the ^{3}He-D_2-filled, 33-μm-thick shells show an improved fusion yield by a factor of 2. The ratio of the measured primary neutron yield to the neutron yield predicted by the hydrodynamics simulation [usually referred to as yield-over-clean (YOC)] is plotted in Fig. 101.14(b) and shows that the 15-atm-D_2-filled, 33-μm-thick shells improve from 0.03 to 0.19. In all cases, the YOC can be seen to improve significantly. The results from high-adiabat implosions with 1-ns square drive pulses are also plotted in Figs. 101.14(a) and 101.14(b). The absolute fusion yield from the 1-ns square data is between yields measured without and with the picket pulse. A high-adiabat implosion will have a lower calculated yield, and therefore the YOC data for the 1-ns square implosions are higher than either the non-picket or picket YOC's.

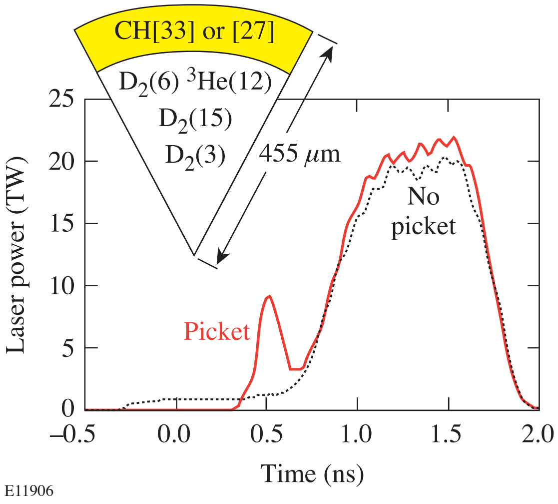

Figure 101.13
Pulse shapes used for decaying-shock-wave picket-pulse experiments. The picket drive is shown as a line and the no-picket drive as a dotted line. The targets used are shown as an inset.

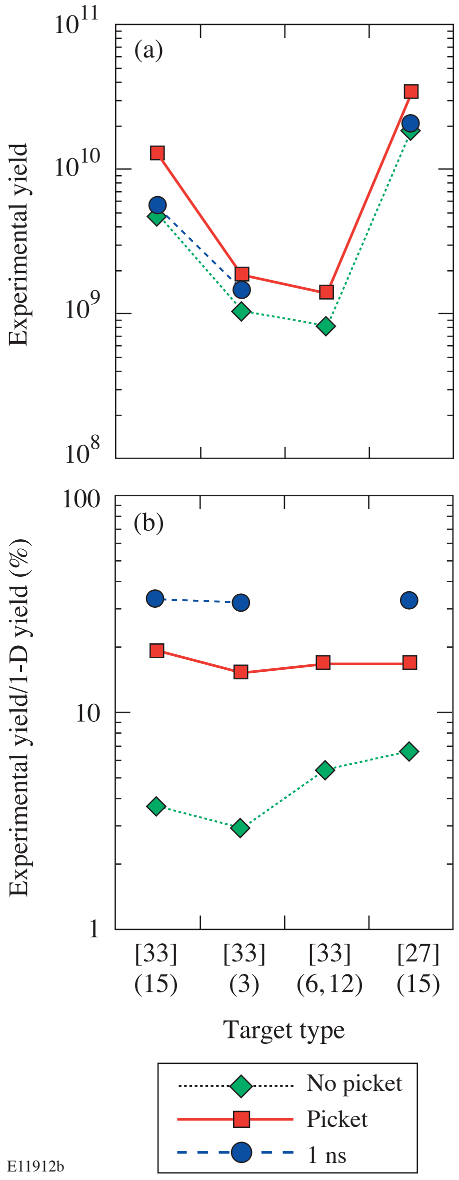

Figure 101.14
Fusion-produced yield from the decaying-shock-wave picket implosions. The absolute yields are shown in (a) and the normalized yields in (b). The picket data are plotted as squares, non-picket data as diamonds, and 1-ns square pulse implosions as circles.

Neutron-production rates for the 15-atm-D_2-filled, 33-μm-thick shell, measured (symbols) and predicted (lines), are shown in Fig. 101.15. The solid curve and open circles are data from the implosion without a picket. The dashed curve and filled circle plots are from the matching implosion using a picket. The experimental data were measured with the "neutron temporal diagnostic" (NTD).[27] The temporal offsets needed to compare experimental and simulation data were determined by maximizing the cross-correlation of the drive portion of the pulse as a function of a temporal shift relative to the laser pulse without a picket. This aligned the leading edges of the main drive pulse for all of the data. It is assumed that the neutron production is determined by the compression of the target by the drive pulse. Comparing the experimental data with predictions indicates that the implosions using a picket not only attain higher absolute yields than the implosions without a picket but also return, as was stated earlier, a larger fraction of the 1-D yield. This suggests more stable implosions with less mix due to RT growth. One-dimensional hydrodynamic simulations indicate that there is little if any adiabat shaping from the picket for these implosions. CH targets are affected by radiation transport that changes the shell adiabat, and this dominates the adiabat from the picket at the time of peak acceleration. Cryogenic D_2 targets will not be dominated by radiation and should show decaying shock-wave adiabat shaping.

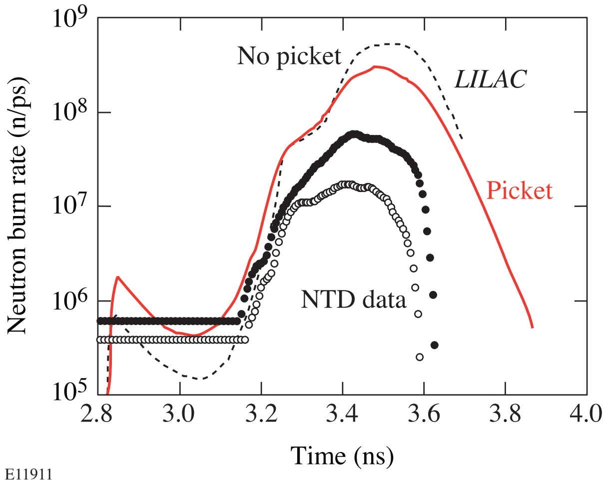

Figure 101.15
NTD data from the decaying-shock-wave implosions. *LILAC* simulation results are plotted for the non-picket pulse (dashed line) and the picket pulse (solid line). Experimental data are plotted for the non-picket pulse (open circles) and the picket drive (dark circles).

The OMEGA laser system was also used to study the effect of relaxation picket target designs on imploding CH shells. A relaxation picket implosion uses a picket in front of a drive pulse that has a high foot intensity. The picket is separated from the drive pulse by a region of zero intensity during which time a rarefaction wave causes the shell to decompress. The non-picket drive is designed to implode the targets on the same adiabat ($\alpha \sim 2$) as that of the inner layer for the relaxation picket. These pulse shapes are shown in Fig. 101.16. The picket pulse had a FWHM of ~60 ps. The targets shown schematically by the inset in Fig. 101.16 were designed for a total laser energy of 18 kJ. They are 870-μm-diam, 35-μm-thick CH shells filled with 15 atm of D_2. A thin (1000-Å) Al layer coated the outside of the targets and was the gas retention barrier.

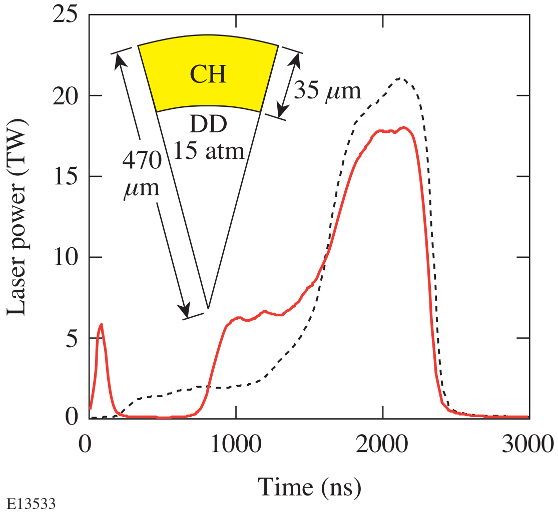

Figure 101.16
Pulse shapes used for relaxation-picket-pulse experiments. The picket drive is shown as the solid line and the non-picket drive as the dashed line. The targets used are shown as an inset.

The measured experimental yields increased when a relaxation (RX) picket pulse was used. The neutron yields shown in Table 101.I were taken for laser drives with and without SSD and with and without a picket pulse. With either SSD on or SSD off, the neutron yields are higher when a picket-pulse drive is used. The yield increases by a factor of 2.5 in the case of SSD off. The laser energy (17.3±0.2 kJ) was very stable for these implosions, allowing for the direct comparison of measured yield data.

Table 101.I: Measured experimental yields increase when a relaxation picket is used.

	SSD Off	SSD On	Clean 1-D
	Yield ($\times 10^9$)	Yield ($\times 10^9$)	Yield ($\times 10^{10}$)
Picket	5.6±0.2	6.8±0.2	5.2±0.5
No picket	2.2±0.1	5.5±0.5	4.0±0.2

One-dimensional hydrodynamic simulations[28] were used to calculate the adiabat shape at the start of acceleration and at peak acceleration shown in Fig. 101.17. *LILAC* simulations indicate that RX adiabat shaping in CH is effective throughout the acceleration phase. The adiabat without a picket pulse is illustrated as the "flat" case. At the start of the shell acceleration the adiabat is nearly constant at $\alpha = 2$ when no picket pulse is used. The RX drive has an adiabat of $\alpha = \sim 12$ at the ablation interface and an $\alpha = 2$ for the inner shell layer. The shape of the adiabat is still steeper for the RX drive at the time of peak acceleration, thus maintaining the effect of a high adiabat at the ablation interface while keeping a low ($\alpha = 2$) adiabat in the shell's interior.

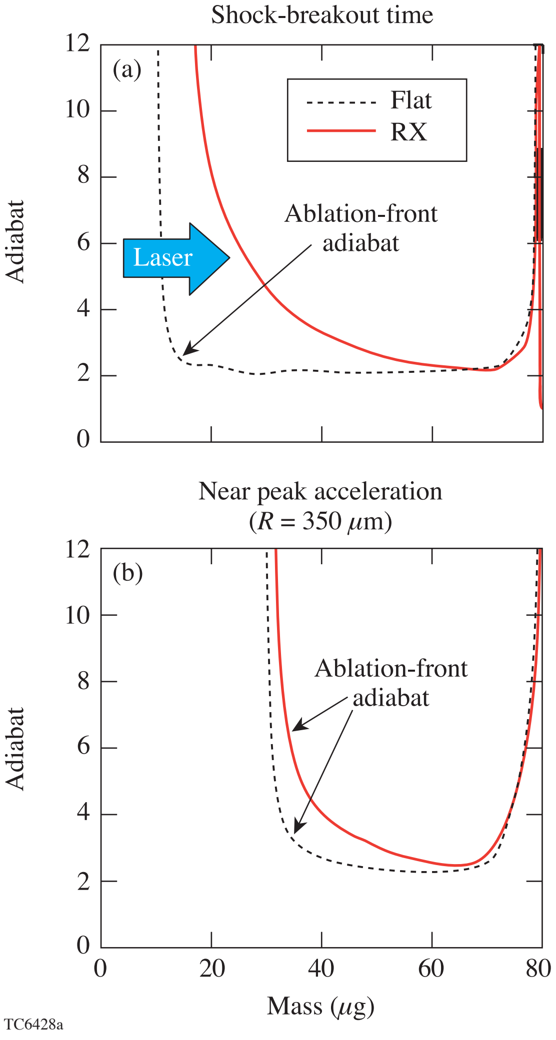

Figure 101.17
Shell adiabat shapes for the relaxation-picket-drive implosions. Shapes for the start of the acceleration are shown in (a) and those for near the peak acceleration are shown in (b). The non-picket drive is shown as a dashed line while the picket-drive profiles are shown as a solid line. The x axis is the Lagrangian mass coordinate.

Extension to Cryogenic Targets

The planar and spherical experimental data can be used to predict the expected performance of cryogenic target picket-pulse implosions. Greater shell stability is predicted for high-performance OMEGA cryogenic target designs with a picket pulse.[18] The decaying-shock-wave picket pulse for a cryogenic target is shown in Fig. 101.18. An OMEGA cryogenic target is typically 860 μm in diameter with a 5-μm-or-less CH shell, with a 65-μm-or-greater DT-ice layer, and a DT-gas pressure determined by the target's temperature. A schematic of this target is shown as the inset in Fig. 101.18. These target implosions are simulated with a drive pulse that has a peak intensity of 30 TW. A 20-TW picket is added for picket implosions. Table 101.II lists the 1-D simulation results. The simulations show that the picket does not compromise the core conditions but improves the shell's integrity. The calculated ρR is 330 mg/cm^2 without the picket and 305 mg/cm^2 with the picket drive. Neutron yields are nearly identical at 6.5×10^{14} and 6×10^{14} without and with the picket, respectively. The shell's stability or integrity is determined by the ratio of the bubble amplitude to the shell thickness. This ratio is greater than 100% for the non-picket implosion and only 55% for the picket implosion.

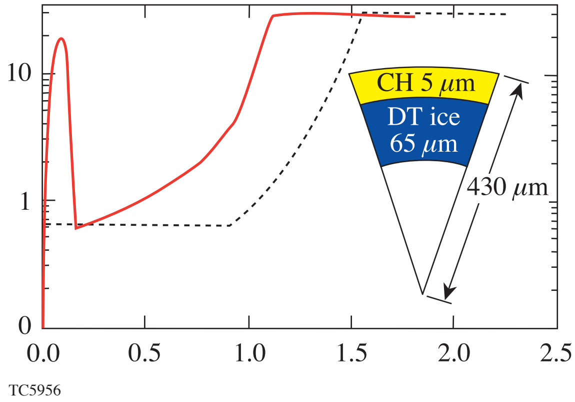

Figure 101.18
Pulse shapes used for cryogenic target simulations. The picket drive is shown as a solid line, and the non-picket drive as a dashed line. The targets used are shown as an inset.

Table 101.II: The decaying-shock-wave picket improves the stability of cryogenic target implosions.

	No Picket	Picket
ρR (mg/cm^2)	330	305
Y ($\times 10^{14}$)	6.5	6
A_{bubble}/Th (%)^1	>100	55

Calculated adiabat and density profiles for both the decaying-shock-wave and relaxation-picket-pulse shapes are shown in Figs. 101.19(a) and 101.19(b). A decaying-shock-wave picket shapes the shell's adiabat [Fig. 101.19(a)] for a cryogenic target at the start of acceleration. The average adiabat for the ablated mass and the inner mass can be calculated from the simulation output. The average ablated mass adiabat calculated for the adiabat shape at the start of acceleration is 8 and the average inner adiabat is 5. At the end of the acceleration phase the average shell adiabat is 5; therefore, the cryogenic target was imploded with a higher ablation interface adiabat than the interior shell adiabat. The relaxation picket shapes the adiabat of the shell at the onset of acceleration as shown in

(a) Decaying shock wave

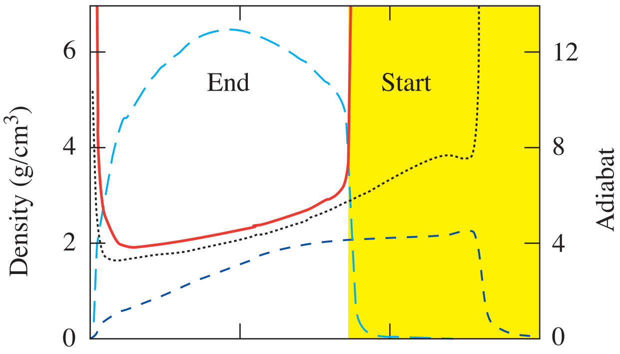

(b) Relaxation picket

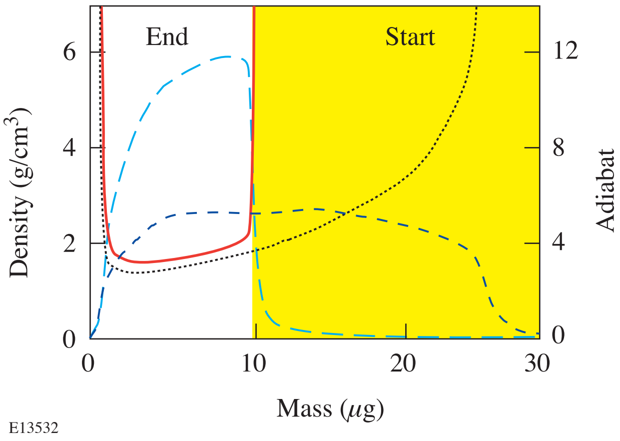

Figure 101.19
Shell adiabat and density shapes for the cryogenic target simulations. Shapes for the decaying-shock-wave picket at the start and end of shell acceleration are shown in (a) and those for the relaxation picket are shown in (b). The non-picket drive adiabat is shown as a solid line while the picket drive adiabat profiles are shown as a dotted line. The density profiles for the non-picket drive are shown as the long-dashed curves and density profiles for the picket drive are shown as the short-dashed curves. The shaded region represents the ablated mass.

Fig. 101.19(b). The RX drive simulations are also used to calculate the average adiabats for the ablated mass and the shell's interior. The shell's adiabat varies from $\alpha = 16$ at the ablation interface to $\alpha = 3$ in the shell's interior. The average adiabat for the ablated mass is 12 and for the inner shell is 3 at the start of shell acceleration. The average shell adiabat at the end of shell acceleration is 4. Both the decaying-shock-wave and the RX picket pulses shape the shell's adiabat for OMEGA cryogenic targets.

Conclusions

Picket pulses coupled to a low-adiabat drive pulse reduce both imprinting and perturbation growth. Adiabat shaping has the potential to improve target stability without significantly increasing the energy needed for compression and ignition. The ablation surface has a high adiabat to increase the ablation velocity and therefore reduce the RT growth. This is done while maintaining the inner portions of the shell on a low adiabat so that the energy needed to compress the core is minimized. The adiabat can be shaped either by launching a decaying shock wave that has a high pressure at the ablation surface and a low pressure at the inner shell surface or by using a picket pulse to produce a spatial density distribution so that a strong shock wave propagating from the ablation interface to the inner shell surface produces an adiabat that is high in the ablated material and low in the compressed material.

Planar experiments with picket pulses have reduced RT growth and imprinting, and spherical experiments with picket pulses show increased fusion yields when a picket pulse is used. With a picket-pulse intensity equal to 50% of the drive-pulse intensity, the RT growth was reduced for a 20-μm-wavelength surface perturbation and no significant RT growth was measured for a picket intensity equal to 100% of the drive pulse. Imprint experiments demonstrated that picket pulses were as effective as 1-D, 1.5-Å SSD at the reduction of imprint for both 60-μm- and 30-μm-wavelength perturbations. Spherical target experiments were done with picket pulses that generate a decaying shock wave and a relaxed density profile. The yields of fusion products are improved both in terms of the absolute value and in terms of the comparison to 1-D hydrodynamic simulation output for the decaying-shock-wave picket, and the absolute yield increased with SSD on and SSD off when the relaxation picket was used.

One-dimensional and two-dimensional hydrodynamic simulations with cryogenic targets show that performance is expected to improve when either the decaying shock wave or the relaxation picket pulse is used. The shell's adiabat can be shaped with either the decaying-shock-wave picket or the relaxation-picket-pulse shape. There is little difference between the core conditions with the flat-shell adiabat or the shaped-shell adiabat, but the ratio of the bubble amplitude to shell thickness is ~55% when the picket is added to the drive.

Results with warm CH targets and calculations with cryogenic targets indicate that picket pulses can be used for NIF direct-drive implosions. Either the decaying-shock-wave or the relaxation-picket-pulse shape can be used to improve the likelihood of achieving ignition.

ACKNOWLEDGMENT

This work was supported by the U.S. Department of Energy Office of Inertial Confinement Fusion under Cooperative Agreement No. DE-FC52-92SF19460, the University of Rochester, and the New York State Energy Research and Development Authority. The support of DOE does not constitute an endorsement by DOE of the views expressed in this article.

REFERENCES

1. J. Nuckolls *et al.*, Nature **239**, 139 (1972).
2. M. C. Herrmann, M. Tabak, and J. D. Lindl, Nucl. Fusion **41**, 99 (2001).
3. R. Betti, K. Anderson, V. N. Goncharov, R. L. McCrory, D. D. Meyerhofer, S. Skupsky, and R. P. J. Town, Phys. Plasmas **9**, 2277 (2002).
4. Lord Rayleigh, Proc. London Math Soc. **XIV**, 170 (1883).
5. G. Taylor, Proc. R. Soc. London Ser. A **201**, 192 (1950).
6. S. E. Bodner, Phys. Rev. Lett. **33**, 761 (1974).
7. J. D. Lindl, in *Inertial Confinement Fusion*, edited by A. Caruso and E. Sindoni (Editrice Compositori, Bologna, Italy, 1989), pp. 595–615.
8. H. Takabe *et al.*, Phys. Fluids **28**, 3676 (1985).
9. R. Betti, V. N. Goncharov, R. L. McCrory, P. Sorotokin, and C. P. Verdon, Phys. Plasmas **3**, 2122 (1996).
10. S. W. Haan, Phys. Rev. A, Gen. Phys. **39**, 5812 (1989).
11. T. J. Kessler, Y. Lin, J. J. Armstrong, and B. Velazquez, in *Laser Coherence Control: Technology and Applications*, edited by H. T. Powell and T. J. Kessler (SPIE, Bellingham, WA, 1993), Vol. 1870, pp. 95–104.
12. Y. Kato, unpublished notes from work at LLE, 1984.
13. T. R. Boehly, V. A. Smalyuk, D. D. Meyerhofer, J. P. Knauer, D. K. Bradley, R. S. Craxton, M. J. Guardalben, S. Skupsky, and T. J. Kessler, J. Appl. Phys. **85**, 3444 (1999).
14. S. Skupsky, R. W. Short, T. Kessler, R. S. Craxton, S. Letzring, and J. M. Soures, J. Appl. Phys. **66**, 3456 (1989).

15. R. H. Lehmberg and S. P. Obenschain, Opt. Commun. **46**, 27 (1983).

16. J. D. Lindl, *Inertial Confinement Fusion: The Quest for Ignition and Energy Gain Using Indirect Drive* (Springer-Verlag, New York, 1998), Chap. 5, p. 54.

17. J. H. Gardner, S. E. Bodner, and J. P. Dahlburg, Phys. Fluids B **3**, 1070 (1991).

18. V. N. Goncharov, J. P. Knauer, P. W. McKenty, P. B. Radha, T. C. Sangster, S. Skupsky, R. Betti, R. L. McCrory, and D. D. Meyerhofer, Phys. Plasmas **10**, 1906 (2003).

19. K. Anderson and R. Betti, Phys. Plasmas **10**, 4448 (2003).

20. K. Anderson and R. Betti, Phys. Plasmas **11**, 5 (2004).

21. J. D. Lindl and W. C. Mead, Phys. Rev. Lett. **34**, 1273 (1975).

22. M. Tabak, Lawrence Livermore National Laboratory, private communication (1987); R. P. J. Town and L. J. Perkins, Lawrence Livermore National Laboratory, private communication (2003).

23. T. J. B. Collins, J. P. Knauer, R. Betti, T. R. Boehly, J. A. Delettrez, V. N. Goncharov, D. D. Meyerhofer, P. W. McKenty, S. Skupsky, and R. P. J. Town, Phys. Plasmas **11**, 1569 (2004).

24. J. P. Knauer, R. Betti, D. K. Bradley, T. R. Boehly, T. J. B. Collins, V. N. Goncharov, P. W. McKenty, D. D. Meyerhofer, V. A. Smalyuk, C. P. Verdon, S. G. Glendinning, D. H. Kalantar, and R. G. Watt, Phys. Plasmas **7**, 338 (2000).

25. T. J. B. Collins and S. Skupsky, Phys. Plasmas **9**, 275 (2002).

26. T. R. Boehly, D. L. Brown, R. S. Craxton, R. L. Keck, J. P. Knauer, J. H. Kelly, T. J. Kessler, S. A. Kumpan, S. J. Loucks, S. A. Letzring, F. J. Marshall, R. L. McCrory, S. F. B. Morse, W. Seka, J. M. Soures, and C. P. Verdon, Opt. Commun. **133**, 495 (1997).

27. R. A. Lerche, D. W. Phillion, and G. L. Tietbohl, in *Ultrahigh- and High-Speed Photography, Videography, and Photonics '93*, edited by P. W. Roehrenbeck (SPIE, Bellingham, WA, 1993), Vol. 2002, pp. 153–161.

28. M. C. Richardson, P. W. McKenty, F. J. Marshall, C. P. Verdon, J. M. Soures, R. L. McCrory, O. Barnouin, R. S. Craxton, J. Delettrez, R. L. Hutchison, P. A. Jaanimagi, R. Keck, T. Kessler, H. Kim, S. A. Letzring, D. M. Roback, W. Seka, S. Skupsky, B. Yaakobi, S. M. Lane, and S. Prussin, in *Laser Interaction and Related Plasma Phenomena*, edited by H. Hora and G. H. Miley (Plenum Publishing, New York, 1986), Vol. 7, pp. 421–448.